An efficient finite–discrete element method for quasi-static nonlinear soil–structure interaction problems

Hoang K. Dang and Mohamed A. Meguid*,†

Department of Civil Engineering and Applied Mechanics, McGill University, Quebec, Canada H3A 2K6

SUMMARY

An efficient finite–discrete element method applicable for the analysis of quasi-static nonlinear soil–structure interaction problems involving large deformations in three-dimensional space was presented in this paper. The present method differs from previous approaches in that the use of very fine mesh and small time steps was not needed to stabilize the calculation. The domain involving the large displacement was modeled using discrete elements, whereas the rest of the domain was modeled using finite elements. Forces acting on the discrete and finite elements were related by introducing interface elements at the boundary of the two domains. To improve the stability of the developed method, we used explicit time integration with different damping schemes applied to each domain to relax the system and to reach stability condition. With appropriate damping schemes, a relatively coarse finite element mesh can be used, resulting in significant savings in the computation time. The proposed algorithm was validated using three different benchmark problems, and the numerical results were compared with existing analytical and numerical solutions. The algorithm performance in solving practical soil–structure interaction problems was also investigated by simulating a large-scale soft ground tunneling problem involving soil loss near an existing lining. Copyright © 2011 John Wiley & Sons, Ltd.

1. INTRODUCTION

The mechanics of soil movement and particle loss near an existing subsurface structure is a challenging soil–structure interaction problem. Standard finite element methods (FEM) are not suitable to analyze these problems because of the unpredictable location and direction of particle movements. In addition, modeling soil behavior following local failure is significantly challenging using FEM. Discrete element method (DEM), on the other hand, has proven to be promising for such analysis as it accounts for the interaction and relative movement of soil particles at the microscale and macroscale levels. Several researchers have successfully used DEM to simulate the response of both laboratory size samples in triaxial compression (e.g. [15]) as well as large-scale applications (e.g. [17]). One of the disadvantages of the DEM is the large amount of calculations needed to model the details of a real geotechnical engineering problem particularly those involving soil–structure interaction. Capturing the soil behavior (e.g. shear band development) at the microscale level in these problems necessitates the use of significantly small particles that could render the cost of the numerical investigation to be practically unfeasible. Therefore, there is a need for the development of a new tool that allows for the analysis of the previous conditions, considering both the microscale and the macroscale features of the problem.

---

*Correspondence to: Mohamed A. Meguid, Department of Civil Engineering and Applied Mechanics, McGill University, 817 Sherbrooke Street West, Montreal, Quebec, Canada H3A 2K6.
†E-mail: mohamed.meguid@mcgill.ca

Oñate and Rojek [21] developed a procedure to combine DEM and FEM for the dynamic analysis of geomechanics problems using an interface at the boundary of the finite element (FE) and discrete element (DE). A similar procedure was developed by Azevedo and Lemos [1], where the forces at the boundary transferred to the FEs are calculated at the interaction points. Both methods were developed in two-dimensional space, and the results obtained from the numerical analysis do not agree well with the experimental data. This was contributed to the fact that the spurious wave reflection at the interface was not considered.

Han *et al.* [13] developed a method to couple FE and DE to simulate the shot peening process; the shot was represented by DE, and the workpiece was modeled using FEs. However, without the treatment of the spurious wave reflection, the size of the FEs at the interface has been reduced to one tenth of the DE, which led to a significant increase in the amount of computation.

Xiao and Belytschko [25] used the bridging domain procedure to couple continuum with molecular models. The spurious wave reflection at the molecular/continuum interface was avoided. A slightly different treatment of the bridging domain was developed by Ben Dhia and Rateau [5] using the so-called *Arlequin method*. The minimum potential energy was applied to all domains. Various authors have used the previously mentioned method in molecular dynamic such as Liu *et al.* [16] and Prudhomme *et al.* [22]. Although it has shown efficiency in reducing the spurious wave reflection, the number of elements used in the analysis increased as well as the complexity of the formulation, which limits the application of the method to effect dynamic problems.

Recently, Fakhimi [12] proposed a combined FE–DE method to simulate a triaxial test such that brick elements were used to simulate the flexible wall around the soil sample. The brick elements were divided into several small tetrahedral elements to prevent the spurious stiffness of the FEs [12], and therefore a significantly large number of FEs were used in the analysis. Because the equations of motion were solved explicitly, the time step was reduced to a very small value, which led to more iterations to reach the desired state.

The aim of this research is to develop an efficient three-dimensional finite–discrete element method to analyze quasi-static problems involving large deformation and failure. In the proposed method, DEs are used to simulate the domain in which large deformation or failure occurs, whereas the rest of the problem is simulated using FEs. The boundary of the FE and DE domains is modeled using interface elements. Suitable damping schemes are applied for each domain to relax the system and to maintain the numerical stability. By using the appropriate damping schemes for each domain, numerical stability has been ensured without decreasing the element size leading to a significant improvement in calculation speed.

The developed algorithm was implemented into the Discrete Element Open Source code YADE [14] integrated with a specifically developed Finite Element Package [9] using C++ programming. An initial condition generation package for the DE [10] was also implemented into the code. Several numerical examples are included to demonstrate the efficiency of the proposed method.

2. GOVERNING EQUATION AND FORCE DESCRIPTION

In deriving the governing equations, the granular material located near a discontinuity was modeled using DEs, whereas FEs were used to simulate the rest of the domain. The central difference time integration scheme is adopted for both FE and DE subdomains, as described in the following sections.

2.1. DE framework

The centered second-order finite difference scheme is used such that the position (orientation) of each particle remains unchanged during each time step and the forces are calculated from the force–displacement relationship. When all forces acting on a particle i are determined, either from other particles or from the boundaries, the problem reduces to the integration of Newton's equations of motion for the translational and rotational degrees of freedom, given by

$$\mathbf{m}_{\mathrm{i}} \frac{d^2}{dt^2} \overrightarrow{\mathbf{r}_i} = \overrightarrow{\mathbf{f}_i} \tag{1}$$

and

$$\mathbf{I}_i \frac{d^2}{dt^2} \overrightarrow{\boldsymbol{\Phi}}_i = \overrightarrow{\mathbf{M}}_i \tag{2}$$

where $\mathbf{m}_i$, $\overrightarrow{\mathbf{r}_i}$, and $\overrightarrow{\boldsymbol{\Phi}}_i$ are the mass, position, and orientation vectors in the space of particle i, respectively. $\mathbf{I}_i$ is the moment of inertia vector of particle i and is defined as

$$\mathbf{I}_i = q_i \mathbf{m}_i (d_i/2)^2 \tag{3}$$

where d_i is the diameter of particle i and q_i is the dimensionless shape factor.

Interactions are short range and active at contacts only, so that the total force (torque) on particle i is $\overrightarrow{\mathbf{f}_i} = \sum_c \overrightarrow{\mathbf{f}_i^c} \left(\overrightarrow{\mathbf{M}}_i = \sum_c \overrightarrow{\mathbf{M}}_i^c \right)$, where the sum runs over all contacts c of particle i. The damping coefficients are applied to forces and moments for computational purposes. Hence, the problems can be solved once all forces acting at the contact (see Figure 1) are determined.

To account for the fact that real grain sizes are much smaller than the spheres used in the analysis and grains are not generally spherical and may exhibit a rough surface texture, the local constitutive model uses the moment transfer law with rolling resistance [2], which was adopted in the present formulation. Despite its simplicity, introducing rolling resistance in the model was found to allow for the mechanical properties of the sand to be captured even when a relatively small number of spherical particles were used in the analysis. The procedure to calculate the contact forces using the moment transfer law is discussed in the next paragraph.

The normal and the tangential forces are calculated as follows:

$$\overrightarrow{\mathbf{f}}_{nci} = K_n \overrightarrow{\Delta}_n \tag{4a}$$

$$\overrightarrow{\mathbf{f}}_{sci} = K_s \delta \overrightarrow{\Delta}_s \tag{4b}$$

where $\overrightarrow{\mathbf{f}}_{nci}$ and $\overrightarrow{\mathbf{f}}_{sci}$ are the normal and tangential forces at contact c of particle i, K_n and K_s are the normal and tangential stiffness at the contact, $\delta \overrightarrow{\Delta}_s$ is the incremental tangential displacement, and $\overrightarrow{\Delta}_n$ is the normal penetration depth between the two particles calculated using

$$\left\| \overrightarrow{\Delta} \right\|_n = 0.5 \times (R_1 + R_2 - O_1 O_2) \tag{5}$$

where R_1 and R_2 are the radii of spheres 1 and 2, respectively, and $O_1 O_2$ is the distance between the centers of the two spheres (Figure 1a).

The stiffness of the two elements in contact is connected in series; thus, K_n and K_s are defined by the following equations:
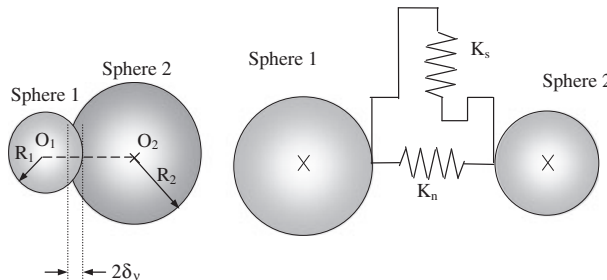

Figure 1. The DE interaction and force-displacement law.

$$K_n = \frac{\frac{k_n^A \times k_n^B}{k_n^A + k_n^B}}{r} \tag{6a}$$

$$K_s = \frac{\frac{k_s^A \times k_s^B}{k_s^A + k_s^B}}{r} \tag{6b}$$

where indices [A] and [B] represent the two spheres in contact; r is the average radius of the two spheres.

$$r = \frac{r_A + r_B}{2} \tag{6c}$$

The shear force is truncated if its absolute value is larger than the maximum value given by Mohr–Coulomb criterion:

$$\overrightarrow{\mathbf{f}}_{sci}^{max} = |\overrightarrow{\mathbf{f}}_{nci}| \times \tan\varphi_i \tag{7}$$

where φ_i is the internal friction coefficient.

The rolling resistance is defined by the component acting in the contact plane. On the other hand, the elastic moment vector M_{elasic}^{L} resulting from the rolling part in the local set of axes is written as

$$M_{elasic}^{L} = k_{ri} \times \boldsymbol{\theta}_{ri}^{L} \tag{8}$$

where k_{ri} is the rolling stiffness defined as

$$k_{ri} = \beta \times K_s \times r^2 \tag{9}$$

where β is a dimensionless coefficient used for the rolling stiffness.

The elastic limit is controlled by the plastic moment vector M_{elasic}^{L} such that

$$\left\| M_{plastic}^{L} \right\| = \eta \cdot r \cdot \left\| \overrightarrow{\mathbf{f}}_{nci} \right\| \tag{10}$$

where η is a dimensionless coefficient used for the plastic moment.

If the elastic limit is reached, the angular rolling vector, $\boldsymbol{\theta}_r$, is computed as

$$\boldsymbol{\theta}_{ri}^{L} = \frac{M_{plastic}^{L}}{k_{ri}} \tag{11}$$

The rolling moment, M_r, in the moment transfer law is defined by the minimal norm of the two moments given by

$$\text{If} \quad \left\| M_{elastic}^{L} \right\| < \left\| M_{plastic}^{L} \right\| : \quad M_i^r = \left\| M_{elastic}^{L} \right\| \quad \text{and} \quad \boldsymbol{\theta}_{ri}^{L} = \frac{M_{elastic}^{L}}{k_{ri}} \tag{12a}$$

$$\text{If} \quad \left\| M_{elastic}^{L} \right\| \geq \left\| M_{plastic}^{L} \right\| : \quad M_i^r = \left\| M_{plastic}^{L} \right\| \frac{M_{elastic}^{L}}{\left\| M_{elastic}^{L} \right\|} \quad \text{and} \quad \boldsymbol{\theta}_{ri}^{L} = \frac{M_{plastic}^{L}}{k_{ri}} \tag{12b}$$

The torque in Equation (2) is then calculated as

$$\overrightarrow{M}_i^c = \overrightarrow{\mathbf{l}_i^c} \times \overrightarrow{\mathbf{f}_i^c} + M_i^r \tag{13}$$

2.2. FE framework

The adaptive dynamic relaxation algorithm previously developed by Dang and Meguid [9] for elasto-plastic geomaterials is used in the present FE formulation. The spatial discretization of a damped structural system can be written as

$$K\mathbf{x} + C\dot{\mathbf{x}} + M\ddot{\mathbf{x}} = \mathbf{P} \tag{14}$$

where K, C, and M are the stiffness, damping, and mass matrices, respectively; $\mathbf{x}$ represents the displacement vector; and $\mathbf{P}$ is the external force vector. The internal force vector $\mathbf{F}$ can be assembled on an element by element basis such that $\mathbf{F} = \int_\Omega B^T \sigma \, d\Omega$, where the B matrix is derived from the shape functions of the element.

To avoid the need for the assembly and factorization of the global matrices, we used a mass proportional damping (cM) together with a diagonal (or lumped) mass matrix (M) obtained. Equation (14) can therefore be written as

$$K\mathbf{x} + cM\dot{\mathbf{x}} + M\ddot{\mathbf{x}} = \mathbf{P} \tag{15}$$

where c is the damping coefficient for mass proportional damping.

2.3. Time step equation

In the central difference method, the velocities are defined at the midpoint of the time step, and the approximation for the temporal derivatives is given as

$$\dot{\mathbf{x}}^{n+1/2} = \frac{1}{\Delta t}\left(\mathbf{x}^{n+1} - \mathbf{x}^{n}\right) \tag{16}$$

$$\ddot{\mathbf{x}}^{n} = \frac{1}{\Delta t}\left(\dot{\mathbf{x}}^{n+1} - \dot{\mathbf{x}}^{n}\right) \tag{17}$$

where Δt is the fixed time step increment. There are generally two methods to derive an incremental relationship: (i) assuming constant acceleration over Δt and (ii) assuming constant velocity over Δt. In this study, the latter method was adopted and the velocity was taken as the average value over Δt:

$$\dot{\mathbf{x}}^{n} = \frac{1}{2}\left(\dot{\mathbf{x}}^{n+1/2} + \dot{\mathbf{x}}^{n-1/2}\right) \tag{18}$$

2.4. Stability time steps

For the stability of the central difference integrator, the time step for both domains must be smaller than a limit derived based on the well-known Courant–Friedrichs–Lewy condition.

$$\Delta t \leq \frac{2}{\sqrt{\lambda_m}} \tag{19}$$

where λ_m is the maximum eigenvalue. An upper bound to the maximum eigenvalue can be obtained from Gerchgorin's theorem as follows

$$\text{For FEs, } \lambda_m \leq \max \sum_{j=1}^{n} \frac{\left|K_{ij}\right|}{M_{ii}} \tag{20}$$

$$\text{For DEs, } \lambda_m \leq \frac{\max(k_s, k_n)}{\mathbf{m}_i} \tag{21}$$

where K_{ij} is a coefficient in the element consistent tangent stiffness matrix, M_{ii} is the element diagonal (or lumped) mass matrix, k_s and k_n are the tangential and normal stiffness of DEs, respectively, and $\mathbf{m}_i$ is the directional mass vector of the DEs. Stability time step is then taken as the minimum of the two values obtained for FEs and DEs.

2.5. Damping schemes

Because the present study is concerned with static geotechnical problems, damping coefficients are incorporated into the time step equations to return the simulated systems to static condition. Because of the different nature of FEs and DEs, and to ensure numerical stability, two different damping schemes are applied for the two subdomains namely Rayleigh damping [9] and Cundall nonviscous damping [8]. A brief description of the two schemes is provided below.

2.5.1. FE damping. Rapid convergence is usually obtained when the ratio of the maximum to minimum eigenvalues is as small as possible. The optimal convergence condition is reached if

$$c \leq 2\sqrt{\lambda_0} \tag{22}$$

where λ_0 is the minimum eigenvalue. To estimate the minimum eigenvalue, the mass-stiffness Rayleigh quotient can be used such that

$$\lambda_0 \cong \frac{\left(\dot{\mathbf{x}}^{n-1/2}\right)^T S^n \dot{\mathbf{x}}^{n-1/2}}{\left(\dot{\mathbf{x}}^{n-1/2}\right)^T M \dot{\mathbf{x}}^{n-1/2}} \tag{23}$$

where S is the lumped stiffness matrix for linear problems. Lumped stiffness matrix is calculated similar to the lumped mass matrix. For nonlinear problem, S^n is determined as follows:

$$S^n \cong \frac{\mathbf{F}^n - \mathbf{F}^{n-1}}{\Delta t \dot{\mathbf{x}}^{n-1/2}} \tag{24}$$

where $\mathbf{F}^n$ and $\mathbf{F}^{n-1}$ are the element internal force vectors at time step n and $n-1$, respectively

No additional parameters are required because the algorithm automatically adjusts the optimal damping coefficient and the time step on the basis of the changes in the element consistent tangent stiffness.

Having the damping coefficient c, substituting Equations (16)–(18) into Equation (15), the expressions for advancing the velocity and displacement vectors, respectively, can be written as

$$\dot{\mathbf{x}}^{n+1/2} = \frac{2 - \Delta tc}{2 + \Delta tc} \left(\dot{\mathbf{x}}^{n-1/2}\right) + \frac{2\Delta t}{2 + \Delta tc} M^{-1}(\mathbf{P}^n - \mathbf{F}^n) \tag{25}$$

$$\mathbf{x}^{n+1} = \mathbf{x}^n + \Delta t \dot{\mathbf{x}}^{n+1/2} \tag{26}$$

where $\mathbf{F}_n$ and $\mathbf{P}_n$ are the internal and external force vectors, respectively, at time step increment n. The inverse of M matrix is trivial because M is diagonal.

2.5.2. DE damping. In the Cundall nonviscous damping, the energy is dissipated by effectively damping the equations of motion. A damping-force term is added to the equations of motion, such that Equations (1) and (2) for each element can be written as

$$\mathbf{m}_i \frac{d^2}{dt^2} \overrightarrow{\mathbf{r}_i} = \overrightarrow{\mathbf{f}_i}(1 - c_f) \tag{27}$$

and

$$\mathbf{I}_i \frac{d^2}{dt^2} \overrightarrow{\mathbf{\Phi}}_i = \overrightarrow{\mathbf{M}}_i(1 - c_m) \tag{28}$$

where c_f and c_m are the force and momentum damping coefficients, respectively.

3. INTERFACE

3.1. Interface generation

The interaction surfaces can be discretized into three-node triangular elements or four-node quadrilateral elements, depending on the element used in the FE domain. The interfaces (or facets) are defined as elements used to transmit the forces between DEs and FEs. In the first case, the triangular facet is defined by the three nodes of the triangular element. In the latter case, all quadrilaterals are broken up into four triangular facets (Figure 2), by creating temporary center node (O), defined by

$$\mathbf{x}^{(O)} = \frac{1}{4} \sum_{i=1}^{4} \mathbf{x}^{(i)} \tag{29}$$

When the four nodes are not located in the same plane, it is obvious that the four triangles will not add geometrically to the original quadrilateral. This procedure was used by Doghri *et al.* [11]. The complicated mapping inversion for quadrilateral facet is also considered to be a disadvantage.

In this study, all facets are implicitly three-node triangles, with nodes numbered 0, 1, and 2 unless otherwise indicated. Consider a three-node triangular facet A as show in Figure 3, the tangential base of the facet is augmented by an outward normal given by

$$\overrightarrow{\mathbf{n}}^A = \frac{\overrightarrow{\mathbf{e}_1} \times \overrightarrow{\mathbf{e}_2}}{\left\| \overrightarrow{\mathbf{e}_1} \times \overrightarrow{\mathbf{e}_2} \right\|} \tag{30}$$

where $\overrightarrow{\mathbf{n}}^A$ is the normal vector of facet A and $\overrightarrow{\mathbf{e}_1}$ and $\overrightarrow{\mathbf{e}_2}$ are two edge vectors of the triangle facet defined as
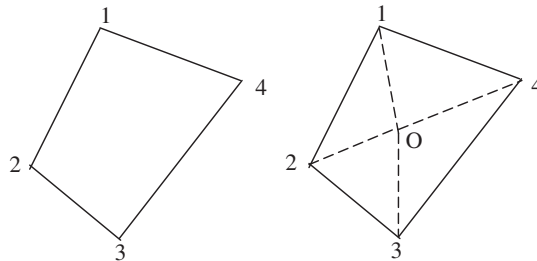

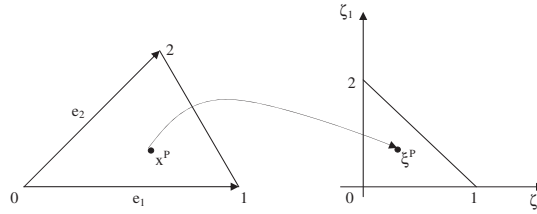Figure 2. Triangular facet setup.

Figure 3. Three-node triangular master facet: projection point, edge vectors and natural coordinate.

$$\overrightarrow{\mathbf{e}_i} = \mathbf{x}^{(i)} - \mathbf{x}^{(0)} \tag{31}$$

Given the facet normal, the projection of any point onto the facet can be easily determined. Now consider a projection (P) of a point onto the interface surface, A is the facet element to which it belongs, and ξ represents its natural coordinates. The mapping FE interpolation gives

$$\mathbf{x}^{(P)} = \sum_{i=0}^{2} N_i \mathbf{x}^{(i)} \tag{32}$$

where the shape functions N_i are defined with respect to the natural coordinates of the projection point

$$N_0 = 1 - \xi_1^P - \xi_2^P, \ N_1 = \xi_1^P, \ N_2 = \xi_2^P \tag{33}$$

3.2. Geometrical parameters for the contact constitutive law

The use of combined FE–DE models involves treatment of the contact between the spherical DEs and the facets. The contact force between the sphere and the facet is decomposed into normal and tangential components. Depending on the contact constitutive law, the contact model between the DE and the facet may include cohesion, damping, friction, wear, heat generation, and exchange. However, the geometrical parameters needed for the constitutive models generally include the contact normal vector, the normal penetration depth (or the gap between a sphere and the facet in case of cohesive law), and the relative and rotational velocities at the contact point. The procedures to derive these quantities are discussed in the next section.

3.2.1. Contact detection. A two-stage contact detection algorithm is used in this research. The set of potential contacts between objects is first obtained through spatial sorting, and then in the second stage, the specific parameters needed for the constitutive law is determined. Various methods of spatial sorting such as the grid method, the octree technique, and the body-base approach have been reported in the literature [19, 20]. As soon as a sphere and a facet are detected in possible contact (see Figure 4), the gap value is calculated as

$$g = \left(\mathbf{x}^{(C)} - \mathbf{x}^{(0)}\right) \cdot \overrightarrow{\mathbf{n}}^A \tag{34}$$

where $\mathbf{x}^{(C)}$ is the coordinate of the sphere center and $\mathbf{x}^{(O)}$ is the coordinate of vertex O.

The first test is then carried out such that

$$\text{No contact if } g > R \tag{35}$$

where R is the sphere radius.

In case of the gap value less than the sphere radius, the natural coordinates of the projection of the sphere center on the facet are calculated as
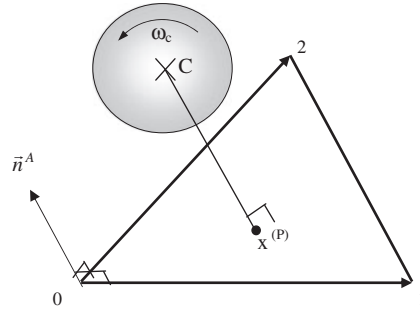
Figure 4. Contact between a sphere and a facet.

$$\xi_1^{(P)} = \frac{\overrightarrow{\mathbf{w}}_2 \cdot \left(\mathbf{x}^{(S)} - \mathbf{x}^{(0)}\right)}{\overrightarrow{\mathbf{w}}_2 \cdot \overrightarrow{\mathbf{e}}_1} \quad \text{and} \quad \xi_2^{(P)} = \frac{\overrightarrow{\mathbf{w}}_1 \cdot \left(\mathbf{x}^{(S)} - \mathbf{x}^{(0)}\right)}{\overrightarrow{\mathbf{w}}_1 \cdot \overrightarrow{\mathbf{e}}_2} \tag{36}$$

where $\overrightarrow{\mathbf{w}}_1$ and $\overrightarrow{\mathbf{w}}_2$ are dual basic defined as

$$\overrightarrow{\mathbf{w}}_1 = \overrightarrow{\mathbf{n}}^A \times \overrightarrow{\mathbf{e}}_1 \text{ and } \overrightarrow{\mathbf{w}}_2 = \overrightarrow{\mathbf{n}}^A \times \overrightarrow{\mathbf{e}}_2 \tag{37}$$

There are three possible cases of a sphere in contact with a facet: (i) a sphere contacts a facet surface, (ii) a sphere contacts a facet edge, and (iii) a sphere contacts a facet vertex. Each case is examined explicitly to ensure numerical stability.

3.2.2. Evaluating contact points, contact normal, and normal penetration depth

3.2.2.1. Surface contact. The contact conditions between a sphere and a facet surface is defined as

$$\text{Surface contact exists if} \quad \begin{cases} 0 < \xi_1^{(P)} < 1 & \text{and} \\ 0 < \xi_2^{(P)} < 1 & \text{and} \\ 0 < \xi_1^{(P)} + \xi_2^{(P)} < 1 \end{cases} \tag{38}$$

As suggested by Doghri [11], taking average normals at all nodes introduces some smoothness in the contact procedure and improves the stability of the contact algorithm; the normal $\mathbf{n}^{(i)}$ to each node excluding the temporary center nodes is computed by taking the sum of the normals to all triangular facets attached to the node. The normals are then normalized to construct unit vectors. The normal at the center node is calculated by averaging the normals at the nodes of the original quadrilateral face as

$$\overrightarrow{\mathbf{n}}^{(O)} = \frac{1}{4}\sum_{i=1}^{4}\mathbf{n}^{(i)} \tag{39}$$

A sphere center is then projected on a facet using the average normals at the nodes. The procedure is described as follows:

Compute the normal to the facet: $\overrightarrow{\mathbf{n}}^{\Delta} = \overrightarrow{\mathbf{e}}_1 \times \overrightarrow{\mathbf{e}}_2$

Compute the gap along the normal to the facet: $g_N = \overrightarrow{\mathbf{n}}^{\Delta} \cdot \left(\mathbf{x}^{(C)} - \mathbf{x}^{(0)}\right)$

Construct a triangle that contains the sphere center and is parallel to the given facet. Nodes of the new triangle are denoted by (0*, 1*, and 2*) and are defined as $\mathbf{x}^{(i*)} = \mathbf{x}^{(i)} + g^{(i)}\overrightarrow{\mathbf{n}}^{(i)}$, i = 0, 1, 2, where $\mathbf{n}^{(i*)}$ is the average normal at node (i), and $g^{(i)}$ components are calculated using $g^{(i)} = \frac{g_N}{\mathbf{n}^{(i)} \cdot \mathbf{n}^{\Delta}}$.

Knowing the coKnowing the coordinates of the facet nodes, the natural coordinates of the sphere center projection can be easily found.

The interpolated normal (also the contact normal) at the projection point P (also the contact point, the normal penetration depth (Δ_n), and the contact point coordinates $(\mathbf{x}^{(P)})$ are expressed by

$$\overrightarrow{\mathbf{n}}^{(P)} \left\| \overrightarrow{\mathbf{n}}^{(P)} \right\| = \sum_{i=0}^{2} N_i \overrightarrow{\mathbf{n}}^{(i)} \tag{40}$$

$$\Delta_n = R - \left(\mathbf{x}^{(C)} - \mathbf{x}^{(P*)} \right) \cdot \overrightarrow{\mathbf{n}}^{(P)} = R - \left(\mathbf{x}^{(C)} - \sum_{i=0}^{2} N_i \mathbf{x}^{(i)} \right) \cdot \overrightarrow{\mathbf{n}}^{(P)} \tag{41}$$

$$\mathbf{x}^{(P)} = \sum_{i=0}^{2} N_i \boldsymbol{\xi}^{(P)} \tag{42}$$

3.2.2.2. Vertex contact. The necessary (but not sufficient) condition that a sphere is in contact with the facet vertex is

$$\text{Vertex contact exists if} \begin{cases} \xi_1^{(P)} = \xi_2^{(P)} & \text{(contact with vertex 0)} \\ \xi_2^{(P)} = 1 - \xi_1^{(P)} - \xi_2^{(P)} & \text{(contact with vertex 1)} \\ \xi_1^{(P)} = 1 - \xi_1^{(P)} - \xi_2^{(P)} & \text{(contact with vertex 2)} \end{cases} \tag{43}$$

The contact normal and the normal penetration depth are given by

$$\overrightarrow{\mathbf{n}}^{(P)} \left\| \overrightarrow{\mathbf{n}}^{(P)} \right\| = \mathbf{x}^{(C)} - \mathbf{x}^{(i)} \tag{44}$$

$$\Delta_n = R - \left(\mathbf{x}^{(C)} - \mathbf{x}^{(i)} \right) \cdot \overrightarrow{\mathbf{n}}^{(P)} \tag{45}$$

where $\mathbf{x}^{(i)}$ is the coordinate of the vertex in contact.

The additional condition for vertex contact is $\Delta_n > 0$. In this case, the contact point is the vertex determined in Equation (43).

3.2.2.3. Edge contact. For all of the other possibilities, a sphere is assumed to be in contact with the facet edge. A quick check is performed to determine the closest edge to the sphere center. The minimum of $\left\{ \left| \xi_1^{(P)} \right|, \left| 1 - \xi_1^{(P)} \right|, \left| \xi_2^{(P)} \right|, \left| 1 - \xi_2^{(P)} \right|, \left| 1 - \xi_1^{(P)} - \xi_1^{(P)} \right|, \left| \xi_1^{(P)} + \xi_1^{(P)} \right| \right\}$ is taken. The conditions to determine the closest edge are

$$
\begin{array}{ll}
\left| \xi_1^{(P)} \right| \ or \ \left| 1 - \xi_1^{(P)} \right| & \text{contact with edge } 0 - 2 \\
\left| \xi_2^{(P)} \right| \ or \ \left| 1 - \xi_2^{(P)} \right| & \text{contact with edge } 0 \text{ and } 1 \\
\left| 1 - \xi_1^{(P)} - \xi_2^{(P)} \right| \ or \ \left| \xi_1^{(P)} + \xi_2^{(P)} \right| & \text{contact with edge } 1 \text{ and } 2
\end{array}
\tag{46}
$$

The projection point P (or the contact point) of the sphere center C with the edge (*mn*) is calculated using

$$\mathbf{x}^{(P)} = \mathbf{x}^{(m)} + \frac{\overrightarrow{\mathbf{x}}^{(C)} \cdot \left(\overrightarrow{\mathbf{x}}^{(n)} - \overrightarrow{\mathbf{x}}^{(m)} \right) - \overrightarrow{\mathbf{x}}^{(m)} \cdot \left(\overrightarrow{\mathbf{x}}^{(n)} - \overrightarrow{\mathbf{x}}^{(m)} \right)}{\left\| \overrightarrow{\mathbf{x}}^{(n)} - \overrightarrow{\mathbf{x}}^{(m)} \right\|^2} \qquad (47)$$

where $\overrightarrow{\mathbf{x}}^{(m)}$, $\overrightarrow{\mathbf{x}}^{(n)}$, and $\overrightarrow{\mathbf{x}}^{(C)}$ are the vector coordinates of points m, n, and C, respectively.

The contact normal and the normal penetration depth are calculated as

$$\overrightarrow{\mathbf{n}}^{(P)} \left\| \overrightarrow{\mathbf{n}}^{(P)} \right\| = \mathbf{x}^{(C)} - \mathbf{x}^{(P)} \qquad (48)$$

$$\Delta_n = R - \left(\mathbf{x}^{(C)} - \mathbf{x}^{(P)} \right) \cdot \overrightarrow{\mathbf{n}}^{(P)} \qquad (49)$$

The additional condition for edge contact is $\Delta_n > 0$.

3.2.3. Additional parameters. Besides the geometric and the material parameters used in the constitutive law, other parameters can generally be derived from the relative and rotational velocities at the contact point. The velocity at the contact point can be interpolated from the velocity of the facet nodes such that

$$\overrightarrow{\dot{\mathbf{u}}}^{(P)} = \sum_{i=0}^{2} N_i \overrightarrow{\mathbf{u}}^{(i)} \qquad (50)$$

where $\overrightarrow{\mathbf{u}}^{(i)}$ is the velocity at node i of the facet. For quadrilateral elements, the velocity of the center node 0 is taken as the average velocity of the quadrilateral nodes to which the facet attaches. The relative velocity at the contact can be calculated using

$$\overrightarrow{\mathbf{u}}_r = \left(\overrightarrow{\dot{\mathbf{u}}}^{(C)} + R \times \to \omega^{(C)} \times \overrightarrow{\mathbf{n}}^{(P)} \right) - \left(\overrightarrow{\dot{\mathbf{u}}}^{(P)} \right) \qquad (51)$$

and the angular velocity of the facet can be calculated based on Fakhimi [12] as

a) Problem definition

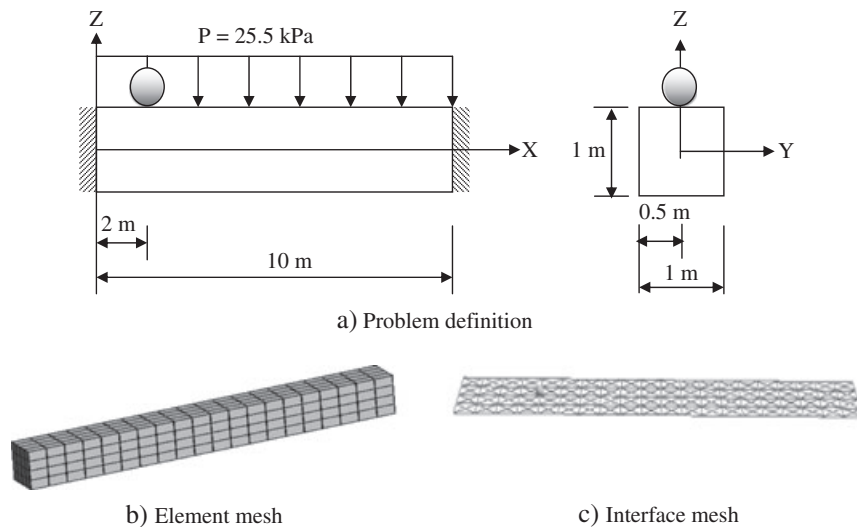b) Element mesh

c) Interface mesh

Figure 5. Fixed beam under uniform loading.

Table I. Material properties used in the model validation.

Case		Poisson's ratio	Young's modulus (Pa)	Unit weight (kN/m³)	Density (kg/m³)
Fixed beam	Beam	0.25	30×10^6	0	2600
	Interface	0.25	30×10^6	0	2600
Simply support plate	Plate	0.2	150×10^6	0	2600
	Interface	0.2	150×10^6	0	2600

$$\boldsymbol{\omega}_i = \frac{1}{2}\left(\dot{\mathbf{u}}_{(k,j)} - \dot{\mathbf{u}}_{(j,k)} \right) \tag{52}$$

where i, j, and k are the 0, 1, and 2 directions. The quantities $\dot{\mathbf{u}}_{(i,1)}$, $\dot{\mathbf{u}}_{(i,2)}$, and $\dot{\mathbf{u}}_{(i,3)}$ can be calculated on the basis of the nodal velocities (see Figure 3 for node denotation) and the facet normal n

$$\left\{ \begin{array}{c} \dot{\mathbf{u}}_i^{(2)} - \dot{\mathbf{u}}_i^{(1)} \\ \dot{\mathbf{u}}_i^{(0)} - \dot{\mathbf{u}}_i^{(2)} \\ 0 \end{array} \right\} = \left[\begin{array}{ccc} \mathbf{x}_1^{(2)} - \mathbf{x}_1^{(1)} & \mathbf{x}_2^{(2)} - \mathbf{x}_2^{(1)} & \mathbf{x}_3^{(2)} - \mathbf{x}_3^{(1)} \\ \mathbf{x}_1^{(0)} - \mathbf{x}_1^{(2)} & \mathbf{x}_2^{(0)} - \mathbf{x}_2^{(2)} & \mathbf{x}_3^{(0)} - \mathbf{x}_3^{(2)} \\ \mathbf{n}_1 & \mathbf{n}_2 & \mathbf{n}_3 \end{array} \right] \left\{ \begin{array}{c} \dot{\mathbf{u}}_{(i,1)} \\ \dot{\mathbf{u}}_{(i,2)} \\ \dot{\mathbf{u}}_{(i,3)} \end{array} \right\} \tag{53}$$

3.3. Force distribution

When all the parameters required for the constitutive law are determined as described earlier, the forces acting at the contact can be calculated (i.e. using Equations (4a), (4a), (5), and (7)). The forces is then distributed to the nodes as follows

$$\mathbf{F}_i = \mathbf{f}_{\text{contact}} N_i \tag{54}$$

where $\mathbf{F}_i$ is the nodal force at node i, $\mathbf{f}_{\text{contact}}$ is the contact force, and N_i is the shape function obtained using the natural coordinates of the contact point $\xi^{(P)}$. If quadrilateral elements are used at the interacting surface, the nodal forces at node 0 (or the center node of the facet) are distributed equally to all nodes of the element.

3.4. Numerical improvement

There are cases where a sphere is found to be in contact with more than one facet at a common edge or corners at a given time step. In the following time step, the sphere may be in contact with only one facet with almost the same geometric parameters. As a result, the forces acting on the sphere and the facet nodes will jump dramatically (i.e. the force magnitude reduces and changes direction if the sphere is in contact with two facets in a previous time step). To improve the smoothness and the numerical stability, we developed a simple and efficient algorithm such that the coordinates of the contact points associated with each sphere are remembered and compared with the others. If the distances among those contact points are less than a certain tolerance, a duplication number (n_d) associated with each contact point is calculated. The forces acting on the sphere and facet nodes are then divided by that number.

$$\mathbf{F} = \mathbf{F}/n_d \tag{55}$$

where $\mathbf{F}$ is the force vector acting on the sphere or the facet node.

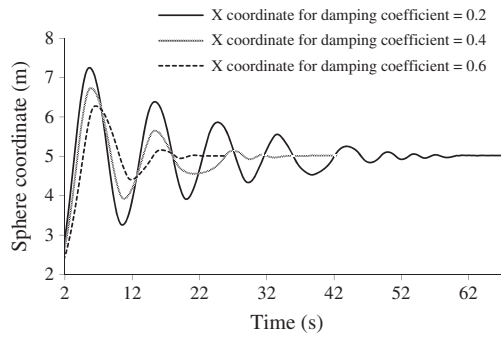Figure 6. Fixed beam: snapshot as the stability condition is reached.

Figure 7. Effect of damping coefficient on the stability of the DE analysis for fixed beam simulation.

4. VALIDATION

The developed algorithm has been validated using two benchmark problems: (1) Fixed beam under uniform loading and (2) Simply supported square plate. Details are given in the next section.

4.1. A sphere over fixed beam

A linear elastic beam with two fixed ends is used to test the response of solid element facets in contact with a spherical particle. A uniform pressure is applied in the negative z direction at the top of the beam as shown in Figure 5a. A sphere with a diameter of 0.1 m is then placed on the surface of the beam. A fictitious weight of 9810 N was assigned to the sphere. As the beam deforms under the applied pressure, the sphere moves along the beam surface until the system reaches stability. A mesh of 4 × 4 × 20 reduced-integration hexahedron elements [3] with hourglass control was used in the simulation (see Figure 5b). An interface mesh that consists of three-node triangles is used as shown in Figure 5c. Material properties used in the analysis are summarized in Table I.

a) Problem definition

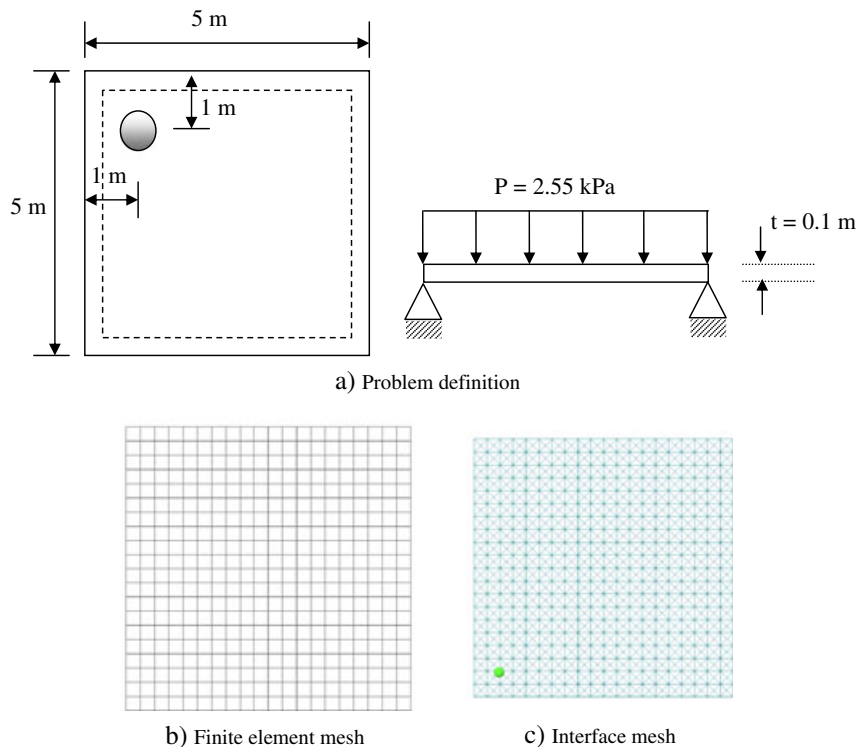b) Finite element mesh

c) Interface mesh

Figure 8. Simply supported square plate: problem description, finite element and interface mesh.
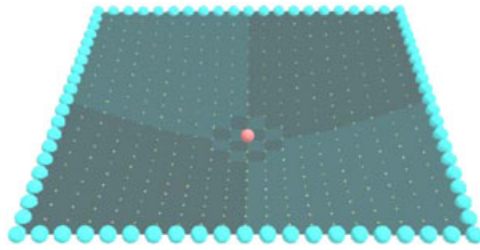
Figure 9. Simply supported square plate: A snapshot as the stability condition is reached.

As stability is reached and because of the symmetry of the deformed shape, the sphere is positioned at the center of the beam as shown in Figure 6. Three simulations were performed using three different values of Cundall's damping coefficient. The beam deflection for all three cases is calculated to be 0.323 m. The theoretical value obtained using direct integration for the same condition is 0.325 m. The effect of the Cundall's damping coefficient is shown in Figure 7. It can be seen that as the damping coefficient increases, the system reaches the stability condition significantly faster.

4.2. Simply supported square plate

A simply supported square plate subjected to a uniform load is analyzed as shown in Figure 8a. Linear elastic material is assumed for the plate. All sides of the plate are simply supported. A sphere 0.1 m in diameter is placed on top of the plate as shown in Figure 8a. A fictitious weight of 9810 N was assigned to the sphere. Similar to the previous example, as the plate deforms under the applied pressure, the sphere moves until the system reaches stability. A mesh of 10×10 one-point quadrature shell elements [4] is used in the analysis (Figure 8b). Each shell element is divided into four triangle facets as shown in Figure 8c. Material properties used in the analysis are summarized in Table I.

A snapshot of the system as the stability condition is reached is shown in Figure 9. The calculated deflection at the center of the plate is found to be 0.725 m, consistent with the analytical solution [24], which predicts a maximum deflection of 0.726 m. Different values of Cundall's damping coefficient were also used in this case and the same maximum deflection was calculated for all the cases.

5. NUMERICAL EXAMPLE

The effect of soil particle loss near an existing tunnel on the stresses in the lining is investigated using the developed algorithm. The problem has been previously investigated using standard FE analyses [18]. However, the analysis was limited to plane strain condition with small voids because of the numerical instability associated with soil failure. The FE analysis considered only voids developed at the tunnel spring line and invert because of the sudden failure that would develop if the void was
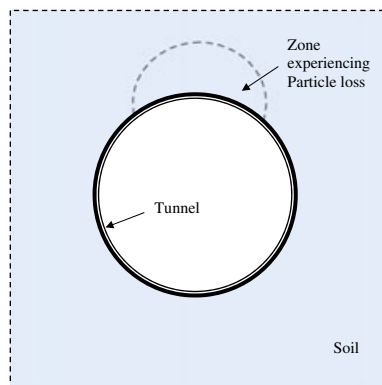

Figure 10. Particle loss zone introduced above an existing tunnel lining.
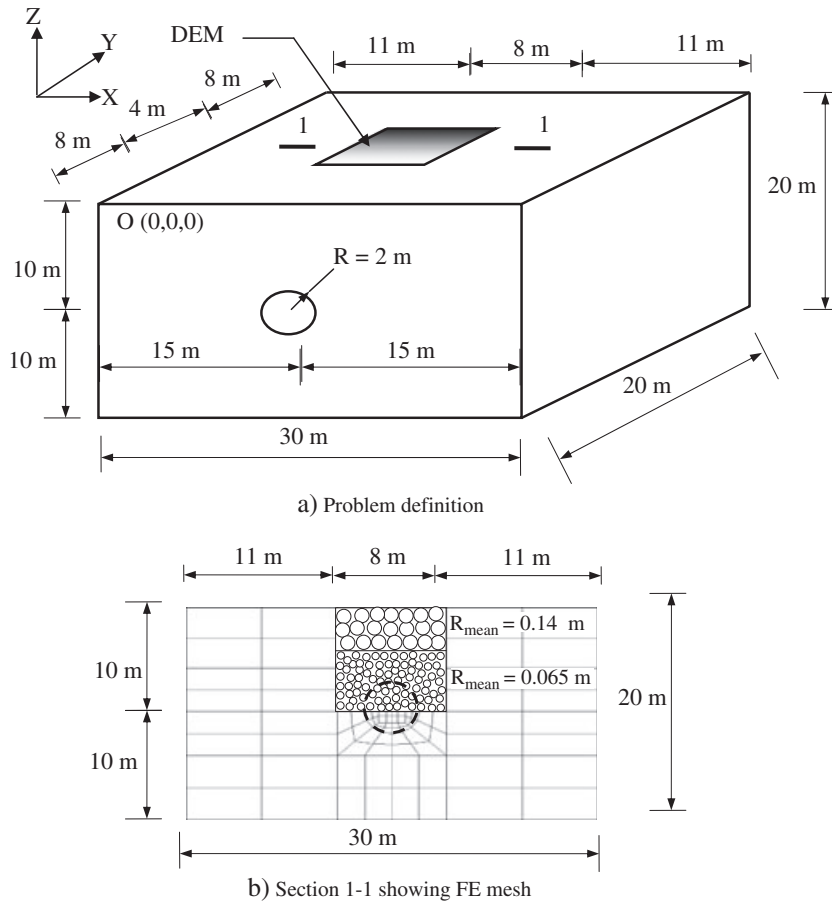
Figure 11. Tunnelling in Mohr-Coulomb soil: Problem definition and finite element mesh.

introduced at the crown. Thus, to demonstrate the efficiency of the developed FE–DE algorithm, numerical analyses have been conducted to evaluate the effects of soil loss induced at the tunnel crown on the stresses in the tunnel lining (see Figure 10). The soil in the particle loss zone (weakened zone) is modeled using DEs and whereas FEs are used to model the rest of the domain.

5.1. Tunneling in Mohr Coulomb material

The first step is to simulate the tunneling procedure and to establish the initial stresses in the soil and lining. The Mohr Coulomb failure criterion with nonassociated flow rule is adopted for the soil medium. The tunnel is assumed to have a circular shape with a diameter of 4 m and located at a depth of 10 m below the ground surface as shown in Figure 11a.

The lining is modeled using the Belytschko–Tsay shell elements with wrap control [4], whereas the soil is modeled using eight-node hexahedron elements with hour glass control [3]. The FE mesh is shown in Figure 11b. The soil volume near the tunnel (from $Y = 8$ m to $Y = 12$ m) is modeled using spherical particles. To reduce the amount of computation, spheres located between $Z = -10$ m

Table II. Material properties used for the FEs.

	Poisson's ratio	Young's modulus (Pa)	Unit weight (kN/m^3)	Friction angle (Degree)	Dilatancy angle (Degree)	Density (kg/m^3)
Soil	0.28	150×10^6	18	30	30	1837
Plate	0.2	20×10^9	25.4	–	–	2600

Table III. The microscopic parameters used for the DEs.

	Normal contact stiffness k_n (Pa)	Ratio $\alpha = \frac{k_s}{k_n}$	Interparticle friction angle μ (degree)	Rolling stiffness coefficient β	Density (kg/m³)
Interface	0.75×10^9	0.02	35	0	N/A
DE	0.75×10^9	0.02	35	0	3070

and $Z = -4$ m have radii that follow a uniform distribution around a mean value of 0.065 m, whereas the spheres located between $Z = -4$ m and $Z = 0$ m have radii that follow a uniform distribution around a mean value of 0.14 m (see Figure 11b). To account for the difference in size of the real grain and the size of the sphere, we used a local moment transfer law discussed in the Section 2.1 [2]. The DE packing is generated using the algorithm developed by the authors and reported elsewhere [10]. Because the scope this paper focuses on combining the DE and the FE, only a brief description will be provided. Details of the algorithms can be found in the previously mentioned reference. The spheres are first generated within a small initial packing. The obtained initial packing is then flipped over the main three axes to produce the flipped sample packing [10]. The final packing is then generated using the flipped sample packing, which produces a final packing having the same structure of the initial packing. Therefore, the calibration process used to determine the DE parameters [2] is only performed on an initial small packing, which leads to significant savings in computational time.

For each face of the hexahedron and shell elements in contact with DEs (see Figures 11a and 11b), four facets are used to model the interface. The entire model is restrained in the horizontal direction at the vertical boundaries (smooth rigid) and is restrained in both the vertical and the horizontal directions at the lower boundary (rough rigid). Fully drained condition is assumed. Material properties used in the
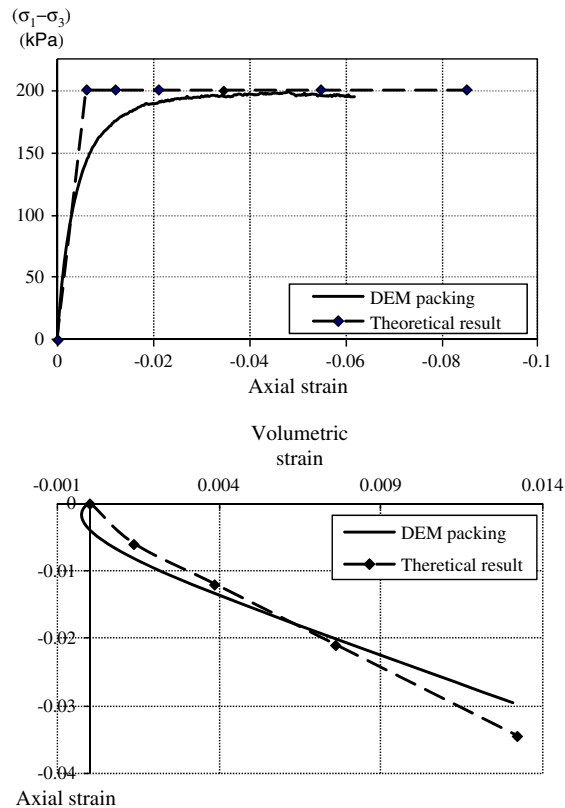

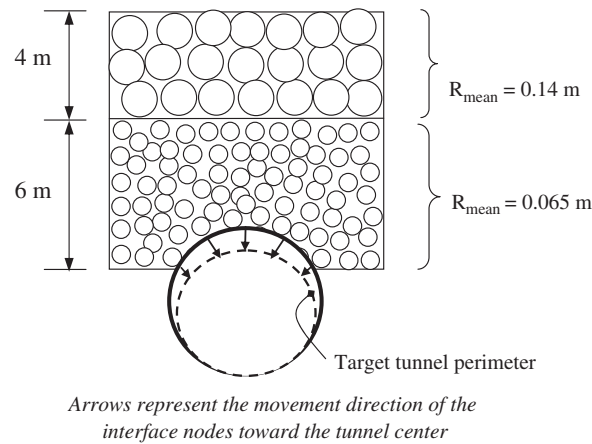Figure 12. Triaxial test results for DEM packing with a confining stress of 100 kPa.

*Arrows represent the movement direction of the
interface nodes toward the tunnel center*

Figure 13. Tunnelling procedure for the DE domain.

analysis are given in Tables II and III. The lateral earth pressure coefficient (K_o) is taken as 0.39. To match the stress strain response of the DEs with FEs, the calibration procedure described by Belheine *et al.* [2] was carried out. Several triaxial tests were performed on the DEs packing to calibrate the DEs properties. The values of $k_s, \alpha = \frac{k_s}{k_n}, \mu, \beta$, and η are determined as given in Table III. With the previously mentioned input values, the response of the triaxial test of DEs packing agrees well with the theoretical stress strain behavior of Mohr–Coulomb material used in FE domain (see Figure 12). To maintain a consistent unit weight of the soil, a density of $3070\,\text{kg/m}^3$ is used for the DEs. For the calculation of the initial condition, the shell elements used to model the tunnel lining are kept inactive.

After the initial condition is generated, the soil elements (both FE and DE) inside the tunnel are deactivated. To simulate the volume loss experienced during tunnel excavation [23], we considered both the FE and the DE zones located within the tunnel circumference. The boundary nodes located along the lining within the FE zone are allowed to move freely under the effect of the residual stresses until they reach the target perimeter of the tunnel as shown in Figure 13. In the DE zone, interface elements located along the lining are first activated, and the interface nodes are moved with a predetermined displacement calculated by the displacement of the closest nodes in the FE zone for each time step (Figure 13). The predetermined displacement vector has the same coefficients as the displacement vector of the FE nodes in the plane perpendicular to the tunnel direction while the coefficient in the tunnel direction remains constant. The target perimeter is calculated on the basis of the volume loss value caused by tunneling procedure (the value of 1% of volume loss was taken in this paper). After all nodes reach the target perimeter, the lining (modeled by shell elements) is activated. The simulation is kept running until the stability condition is reached.

To calibrate the program, we compared the calculated thrust forces and moments with the numerical solution obtained using the commercial software Plaxis Tunnel 3D [6] (see Table IV).

Shear force and moment distributions in the tunnel lining are shown in Figure 14. As shown in the figure, the calculated lining force and moment are consistent throughout the lining, including the central section where DEs are used to model the soil above the lining. A smooth transition in both force and moment distributions was observed along the lining calculated for DEs (near the middle of the lining) as well as for the FEs (along the rest of the lining).

Table IV. Comparison of tunnel lining thrust force and moment.

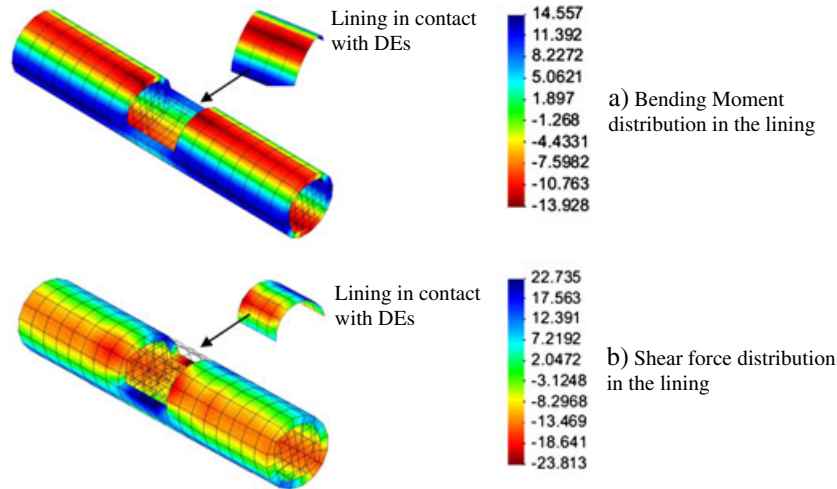| Method	Maximum shear force (kN)	Moment at lining top (kN·m)	Minimum shear force (kN)	Moment at spring line (kN·m)
Plaxis tunnel 3D	22.5	13.865	22.5	14.304
FE–DE	22.735	13.928	23.813	14.557

Figure 14. Bending moment and shear force distributions in the tunnel lining.

5.2. Effects of local soil loss on tunnel lining

After the initial stresses are established, particle loss is induced locally to weaken the soil at the tunnel crown as shown in Figure 10. Although the DEM is capable of modeling the falling of portion of the soil through the lining, an alternative simplified procedure was chosen such that DEs are deactivated and removed from the model within a predefined spherical shaped zone above the lining. This procedure was found to accelerate the calculation process. The center of the spherical zone is located at $X = 15$ m, $Y = -10$ m, and $Z = 10$ m. To simulate the particle loss, we deactivated and removed the DEs within the target zone from the model. The analysis is kept running until the stability condition is reached. Six different sizes of the weakened zone are considered by increasing the radius of the weakened zone in six increments, namely, 0.25, 0.5, 0.75, 1, 1.25, and 1.5 m. The lining forces and moments calculated for the difference cases are presented in Figure 15. The sizes of the weakened zones are normalized with respect to the tunnel circumference and expressed using the ratio ($D_v/\pi D$), where R_v is the zone radius, πD is the lining circumference and D is the tunnel diameter.

As shown in Figure 15, the bending moment at spring line initially increased at a slow rate. This was followed up by a rapid decrease as the size of the weakened zone increased. When the size of the zone reached 12% of the tunnel circumference, the bending moment decreased to approximately 60% of its original value. Bending moment at the crown increased consistently for all the examined zone sizes. Similar trend was also observed for the thrust forces in the lining.
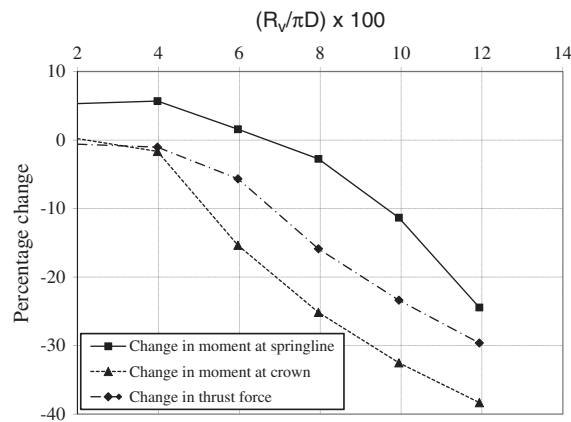

Figure 15. Changes in bending moment and thrust force in the tunnel lining with different void sizes.

6. SUMMARY AND CONCLUSIONS

A combined finite–discrete element method for soil–structure interaction under quasi-static condition was presented. The developed algorithm can be used to combine solid or shell elements with DEs. Rayleigh damping was used for the FE domain whereas the Cundall's damping was used for DE domain. This combination results in a coarser FE mesh and leads to a significant improvement in the computation speed. Numerical simulations were carried out to calibrate the developed algorithm and the results were found to agree well with the analytical solutions as well as other numerical solutions.

A practical example involving soil loss around existing underground tunnel was also presented. The analysis showed the advantages of the developed method in analyzing complicated soil–structure interaction problems under quasi-static condition. With the developed method, the analysis of large-scale problems becomes feasible, inheriting the advantages of both FE and DE methods.

REFERENCES

1. Azevedo NM, Lemos JV. Hybrid discrete element/finite element method for fracture analysis. *Computer Methods in Applied Mechanics and Engineering* 2006; **195**(33–36):4579–4593.
2. Belheine N, Plassiard JP, Donzé FV, Darve F, Seridi A. Numerical simulation of drained triaxial test using 3D discrete element modeling. *Computers and Geotechnics* 2009; **36**(1–2):320–331.
3. Belytschko T, Ong JS-J, Wing Kam L, Kennedy JM. Hourglass control in linear and nonlinear problems. *Computer Methods in Applied Mechanics and Engineering* 1984; **43**(3):251–276.
4. Belytschko T. Advances in one-point quadrature shell elements. *Computer Methods in Applied Mechanics and Engineering* 1992; **96**(1):93–107.
5. Ben Dhia H, Rateau G. The Arlequin method as a flexible engineering design tool. *International Journal for Numerical Methods in Engineering* 2005; **62**(11):1442–1462.
6. Brinkgreve RBJ, Vermeer PA. Plaxis Tunnel 3D Users Manual. Balkema: Rotterdam, 2001.
7. Chaudhary A, Bathe KJ. A solution method for planar and axisymmetric contact problems. *International Journal for Numerical Methods in Engineering* 1985; **21**(1):65–88.
8. Cundall PA, Hart RD. Numerical modeling of discontinua. In Keynote address in Proceedings of the 1st US conference on discrete element methods (Golden Colorado), Mustoe GGW, Henriksen M, Huttelmaier H-P (eds.). CSM Press: Golden Colorado, 1989; 1–17.
9. Dang HK, Meguid MA. Evaluating the performance of an explicit dynamic relaxation technique in analyzing nonlinear geotechnical engineering problems. *Computers and Geotechnics* 2010a; **37**(1–2):125–131.
10. Dang HK, Meguid MA. Algorithm to Generate a Discrete Element Specimen with Predefined Properties. *International Journal of Geomechanics* 2010b; **10**(2):85–91.
11. Doghri I, Muller A, Taylor RL. A general three-dimensional contact procedure for implicit finite element codes. *Engineering Computations* 1998; **15**(2–3):233–259.
12. Fakhimi A. A hybrid discrete-finite element model for numerical simulation of geomaterials. *Computers and Geotechnics* 2009; **36**(3):386–395.
13. Han K, Peric D, Owen DRJ, Yu J. A combined finite/discrete element simulation of shot peening processes - Part II: 3D interaction laws. *Engineering Computations* 2000; **17**:680–702.
14. Kozicki J, Donzé FV. A new open-source software developed for numerical simulations using discrete modeling methods. *Computer Methods in Applied Mechanics and Engineering* 2008; **197**(49–50):4429–4443.
15. Liu SH, Sun DA, Wang Y. Numerical study of soil collapse behavior by discrete element modelling. *Computers and Geotechnics* 2003; **30**(5):399–408.
16. Liu WK, Park HS, Qian D, Karpov EG, Kadowaki H, Wagner GJ. Bridging scale methods for nanomechanics and materials. *Computer Methods in Applied Mechanics and Engineering* 2006; **195**(13–16):1407–1421.
17. Maynar MJM, Rodriguez LEM. Discrete Numerical Model for Analysis of Earth Pressure Balance Tunnel Excavation. *Journal of Geotechnical and Geoenvironmental Engineering* 2005; **131**(10):1234–1242.
18. Meguid MA, Dang HK. The effect of erosion voids on existing tunnel linings. *Tunnelling and Underground Space Technology* 2009; **24**(3):278–286.
19. Munjiza A. The Combined Finite–Discrete Element Method. Wiley: Chichester, 2004.
20. Munjiza A, Rougier E, John NWM. MR linear contact detection algorithm. *International Journal for Numerical Methods in Engineering* 2005; **66**:46–71.

21. Oñate E, Rojek J. Combination of discrete element and finite element methods for dynamic analysis of geomechanics problems. *Computer Methods in Applied Mechanics and Engineering* 2004; **193**(27–29):3087–3128.
22. Prudhomme S, Ben Dhia H, Bauman PT, Elkhodja N, Oden JT. Computational analysis of modeling error for the coupling of particle and continuum models by the Arlequin method. *Computer Methods in Applied Mechanics and Engineering* 2008; **197**(41–42):3399–3409.
23. Rowe RK, Lo KY, Kack GJ. A method of estimating surface settlement above tunnels constructed in soft ground. *Canadian Geotechnical Journal* 1983; **20**(1):11–22.
24. Timoshenko S. Theory of plates and shells McGraw-Hill.: New York, 1959.
25. Xiao SP, Belytschko T. A bridging domain method for coupling continua with molecular dynamics. *Computer Methods in Applied Mechanics and Engineering* 2004; **193**(17–20):1645–1669.